Chemical Engineering Journal 522 (2025) 167301

Contents lists available at ScienceDirect

Chemical Engineering Journal

journal homepage: www.elsevier.com/locate/cej

Molecular architecture strategies for UV-enhanced NO_2 sensors under ambient conditions

Berta Pérez-Román [a,b,*], Jesús López-Sánchez [a], M. Alejandra Mazo [a], Álvaro Peña [c], David G. Calatayud [d], Pilar Marín [c], Laura Pascual [e], Rocío E. Rojas-Hernández [a,f], Daniel Matatagui [c], Fernando Rubio-Marcos [a,**]

[a] Instituto de Cerámica y Vidrio (ICV-CSIC), C/Kelsen 5, 28049 Madrid, Spain
[b] Escuela de Doctorado UAM, Francisco Tomás y Valiente 2, 28049 Madrid, Spain
[c] Instituto de Magnetismo Aplicado, (UCM-ADIF), Departamento de Física de Materiales, Universidad Complutense de Madrid (UCM), 28040 Madrid, Spain
[d] Departamento de Química Inorgánica, Universidad Autónoma de Madrid, Francisco Tomás y Valiente 7, 28049 Madrid, Spain
[e] Instituto de Catálisis y Petroleoquímica (ICP-CSIC), C/Marie Curie 2, 28049 Madrid, Spain
[f] Department of Mechanical and Industrial Engineering, Tallinn University of Technology, Ehitajate 5, 19180 Tallinn, Estonia

ARTICLE INFO

Keywords:
Nitrogen doping
Engineering molecular architecture
Carbide-derived carbons
Ultra-sensitivity
Nitrogen dioxide
Gas sensor

ABSTRACT

Detecting nitrogen dioxide (NO_2) below sub-ppm levels is critical for mitigating health risks associated with air pollution. Carbon-based materials are promising candidates for gas sensing, but their performance depends strongly on structural and chemical tuning. Here we show that nitrogen-doped carbide-derived carbons synthesized using dendritic molecular architectures exhibit enhanced gas-sensing properties. The resulting 2D porous structure demonstrates p-type response to NO_2, with a sensitivity of 7.9 ± 2.8 %/ppm in dark conditions. Under ultraviolet illumination, the response increases by 150 % without inducing poisoning effects. This improvement is attributed to the combined effects of nitrogen doping, high defect concentration, and hierarchical micro-mesoporosity. Our results demonstrate that molecular design is a powerful strategy to engineer carbon materials with tunable gas-sensing properties, offering new opportunities for next-generation detection technologies.

1. Introduction

Reducing the emissions of polluting and harmful gases is urgent because of the growing evidence of their significant impact on the public health, particularly related to cardiorespiratory issues [1]. In this context, nitrogen dioxide (NO_2) is one of the key pollutants that comes from different industries as transportation or power generation that needs to be controlled [2]. The World Health Organization (WHO) has published Global Air Quality Guidelines (AQGs), providing a guidance for air pollution management to achieve an optimal air quality. According to the latest WHO data, the recommended AQGs NO_2 levels are 200 μg/m^3 (≈ 106 ppb) for 1-hour exposure and 25 μg/m^3 (≈ 13 ppb) for 24-hour [3]. Therefore, the need for highly sensitive sensor devices arises due to the challenge of detecting hazardous gases at extremely low concentrations (below 1 ppm) in real-time at room temperature (RT).

To integrate the gas sensor devices into daily life, it is imperative to develop simple, small-sized and portable gas sensors, capable to operate at RT and providing a high resistance towards humidity [4]. Among the different gas sensor configurations, those based on chemiresistive working principle offer notable advantages, including rapid response times, high stability and selectivity, low-cost, ease of production and the potential for miniaturization [5]. Metal oxide semiconductors (MOs) and carbonaceous materials (including two-dimensional materials, 2DMs) are extensively studied as sensing materials, offering cost-effectiveness and high sensitivity solutions [6]. However, MOs often require elevated temperature operations (200–500 °C) to facilitate adsorption processes, implying an external heating source [7]. This aspect complicates their practical applications, hinders miniaturization and reduces long-term stability [8]. Consequently, light activation emerges as an alternative method to thermal heating, promoting changes in the electronic properties by the generation of photo-induced charge carriers [9].

* Correspondence to: B. Pérez-Román, Instituto de Cerámica y Vidrio (ICV-CSIC), C/Kelsen 5, 28049 Madrid, Spain.
** Corresponding author.
E-mail addresses: berta.perez@icv.csic.es (B. Pérez-Román), frmarcos@icv.csic.es (F. Rubio-Marcos).

https://doi.org/10.1016/j.cej.2025.167301
Received 13 May 2025; Received in revised form 23 July 2025; Accepted 15 August 2025
Available online 16 August 2025

MOs sensing materials can be photo-activated, however, they typically require highly energetic ultra-violet (UV) light due to their wide bandgaps. In contrast, carbon-based materials offer significant advantages for light-activated gas sensors because of their narrower bandgaps, which enable the rapid generation of photogenerated energy carriers, increasing the number of active sites with less energetic UV light. In addition, carbon-based structures exhibit interesting properties such as large specific surface areas, and layered structures that enhance their reactivity as gas-sensing materials [10]. For carbon-based gas sensors operated at RT, UV light facilitates the recovery process (τ_{rec}), boosting sensitivity and selectivity, while promoting faster responses [11,12]. Graphene and its derivatives, known for their high carrier mobility (2×10^5 $cm^2/V.s$) and good electrical conductivity, are studied as sensing materials due to low Johnson noise and enhanced responses [13].

To improve the gas sensing performance, doping material with heteroatoms is an efficient strategy, involving noble metals (Pt, Pd, Au, Ag) [14–16], metals (Ni^{2+}, Zn^{2+}, Co^{3+}) [17,18], or other elements, such as B or N [19,20]. These dopants create synergetic effects by forming catalytic sites that promote redox reactions between the target gases and sensing material, facilitating charge transfer and carrier transport, thereby improving sensitivity, selectivity and stability. However, it should be mentioned that the introduction of these heteroatoms have some drawbacks, such as potential agglomeration, toxicity and/or increased production costs [21]. In this context, carbide-derived carbons (CDCs) emerge as promising candidates due to their highly porous nature, which results from the selective etching of metal carbide and silicon oxycarbides structures [22]. Their synthesis process allows a precise control over the microstructure of the CDCs, reaching highly porous carbon-based materials with tuneable properties, in which the incorporation of heteroatoms can be controlled, thus, enhancing their final functionality [23].

In this work, we present UV-light-activated carbon-based sensing materials with high selectivity and sensitivity for the detection of NO_2 at sub-ppm levels. The engineered doping of CDCs with novel dendritic architectures is crucial to improving the capabilities of the gas sensor. These branched dendritic structures incorporate the nitrogen heteroatoms primarily in the graphitic form (graphitic-N), coupled with pyridinic-N and pyrrolic-N. The tailored molecular architecture promotes catalytic reactions, optimizing charge carrier dynamics in response to UV light, resulting in outstanding sensitivity at the sub-ppm level and fast sensor responses. The proposed strategy represents a significant step forward in the development of carbon-based sensing materials for real-time environmental monitoring and early detection of harmful pollutants.

2. Results and discussion

2.1. Characterization of CDC materials

The preparation route of the highly porous N-doped CDC materials is shown in the supplementary information (Fig. S1). In simple terms, three nitrogen-containing dendritic structures are designed and synthesized with varied nitrogen content and functionalities, different molecular arrangements, increasing complexity and branching across three dendritic molecules (from dendron D1 to dendron D3). The design strategies aim to modify the structural and electronic properties, enabling potentially distinct sensor responses to NO_2. In this context, the dendrons are used to promote the incorporation of nitrogen into an allylhydrido polycarbosilane (AHPCS), followed by a pyrolysis treatment to produce the polymer-to-ceramic transformation. N-containing polymer-derived ceramics (N-PDCs) are obtained, mainly constituted by two contributions; (i) a SiO_xC_{4-x} matrix and (ii) a free carbon phase (C_{free}), both characteristic of the carbide-based materials, in which nitrogen introduction is expected to occur in both phases, but with a major presence in the C_{free} phase, as reported in our previous study [24]. Subsequently, the N-PDCs are subjected to a selective etching treatment (chlorination), resulting in highly porous nitrogen-doped CDC materials (1D, 2D and 3D). These materials are synthesized with different dendritic molecules (D1, D2 and D3, respectively), incorporating different nitrogen concentrations and functionalities. It is important to notice that a Ref sample without the addition of any dendron, is made to study the influence of nitrogen doping.

The morphological microstructures of the prepared CDC samples are studied by transmission electron microscopy (TEM). A comparison between the Ref and 2D samples is shown in Fig. 1a-b and Fig. 1d, respectively. In addition, TEM images of the as-synthesized materials at various magnifications are provided in the Supplementary Information (Fig. S2). The TEM images (Fig. S2a-d) show particles with uneven shape and a rough surface in the N-doped materials, particularly evident in the 2D sample (Fig. S2g). In contrast, planar surface particle is observed in the Ref material (Fig. S2a). The elemental maps obtained by energy dispersive X-ray spectroscopy (EDS) of Ref, and 2D samples are displayed in Fig. 1c and Fig. 1e-f. These mappings confirm the presence of carbon and nitrogen atoms and demonstrate the uniform incorporation of nitrogen throughout the 2D sample. Carbon and nitrogen contents are estimated, with traces of residual chlorine (< 0.1 at.%) remaining after the chlorination process (Table S1). As expected, the materials are primarily composed of carbon, highlighting the efficiency of the selective etching treatment employed for the obtaining of the CDCs. Furthermore, N was detected in the different N-doped samples, reaching a maximum N concentration in the 2D sample (~2 at.%), followed by 3D and 1D materials (1.15 and 0.38 at.%), respectively.

The porous structures fundamentally formed during the etching treatment are examined by N_2 adsorption-desorption technique (Fig. 1h). The Ref sample exhibits type-Ia isotherm with an increased adsorption volume at low relative pressures. This behaviour confirms the characteristics of microporous materials [25,26]. In contrast, N-doped CDC samples show type-IVa isotherms with hysteresis loops in the medium to high-pressure regions, denoting the presence of mesoporous (2–50 nm) [25]. This phenomenon is particularly evident in the 2D sample, discerning a larger hysteresis loop, and therefore, higher content of mesoporous. Some macroporous (> 50 nm) are also detected as the increased adsorbed volume at high relative pressures, which coexists with the microporosity already discerned. D1 and D3 samples reveal similar adsorption behaviour, with smaller hysteresis loops and a greater presence of microporous compared to the 2D sample, as reflected in the sharp rise in the low-pressure regions. The pore size distribution curves illustrated in Fig. 1i further highlight that the Ref sample is predominantly microporous, while the N-doped materials exhibit hierarchically porous microstructures with micro-, meso- and macropores, especially noticeable for the D2 sample.

A deeper insight into the textural analysis is performed, assessing the adsorbed volumes of micro-, meso- and macropores (V_{micro}, V_{meso}, and V_{macro}), as summarized in Table S2. The 2D sample shows higher V_{meso} (0.15 cm^3/g) and V_{macro} (0.08 g/cm^3) values compared to 1D and 3D materials, which have V_{meso} of 0.09 and 0.10 g/cm^3, and V_{macro} of 0.03 and 0.04 g/cm^3, respectively. These results suggest that the organic molecules induce the formation of larger pore sizes (meso-macropores), coexisting with the microporosity primarily originating from the chlorine etching of the PDC structure obtained from the pyrolysis of the AHPCS [27,28]. Consequently, the specific surface areas (S_{BET}) shown in Fig. 1j, are below 2100 m^2/g for the Ref and 2D samples. However, 1D and 3D materials exhibit higher S_{BET} values (> 2690 m^2/g) because of the larger microporosity induced in these samples.

From a long-range order perspective, the XRD diffraction patterns do not exhibit crystalline peaks (Fig. S2i), denoting the formation of highly amorphous structures due to the low pyrolysis temperatures. In this sense, a broad shoulder centred around $2\theta = 5°$ is distinguished in all samples, evidencing the greater formation of porosity during etching which is enhanced by the introduction of the organic molecules in the AHPCS [29], especially for D2 sample. Its relative intensity increases from the Ref material to the N-doped samples, obtaining larger porous

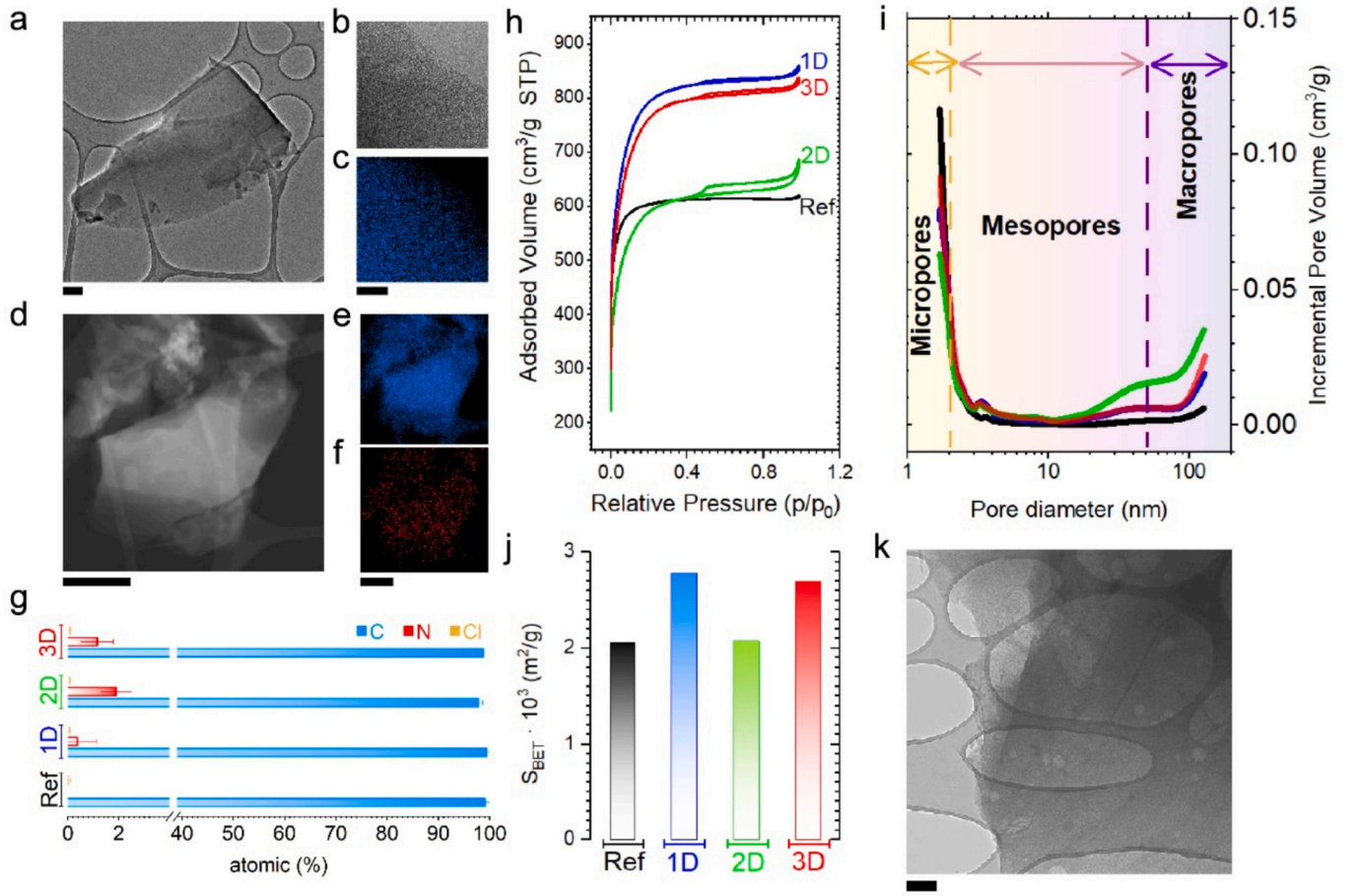

Fig. 1. Microstructural, compositional, and textural characterization. a. TEM, b. HRTEM, and c. Carbon elemental map of Ref sample (un-doped). *Scale bars, 200 nm and 20 nm, respectively*. d. ADF-STEM, e. Carbon, and f. Nitrogen elemental maps of 2D sample. *Scale bars, 200 nm.* g. Atomic percentage obtained from EDS-TEM analysis. h. Nitrogen adsorption-desorption isotherms. i. Pore size distribution curves of the set of samples and j. S_{BET}. k. TEM image of 2D material. *Scale bar, 200 nm.* Notice that carbon (C) and nitrogen (N) are shown in panels c, e, f, and g in bluish and reddish colour, respectively.

structures in the 2D sample (as also shown in Fig. 1k), followed by 1D and 3D materials. These findings are consistent with the elevated mesopore volume values reported in Table S2.

Confocal Raman microscopy is used to deeper insight into the nature and concentration of defects presented in the carbonaceous derived materials. The average Raman spectra and their corresponding Voigt curve fitting are presented in Fig. 2a-d, with the spectra corresponding to highly disordered carbon in accordance with the low pyrolysis temperature employed for the preparation of the materials [24]. In turn, the average Raman spectra and their deconvolution are provided in Fig. S3 and Table S3 (Supplementary Information). As shown in Fig. 2a-d, Raman spectra can be explained by four peaks known as; D* (~1200 cm^{-1}), D (~1340 cm^{-1}), D″ (~1535 cm^{-1}) and G (~1600 cm^{-1}) [30,31]. Specifically, D band is activated by the presence of defects into the sp^2 carbon phase, representing the breathing mode of the carbon rings (A_{1g}-symmetry of disordered graphitic lattice), while G band corresponds to the E_{2g}-symmetry in an ideal graphitic lattice [32]. Interestingly, D* band indicates the presence of impurities or symmetry disruption, typically attributed to heteroatoms in the carbonaceous structures, e.g. nitrogen and oxygen atoms [33]. In contrast, D″ band can be related to topological defects in the carbon rings, as the pentagon carbon defects [34].

Peak intensity refers to the height of the deconvoluted Raman modes and is collected in Table S3. From the peak intensity ratio, I_D/I_G, the defect concentrations can be estimated, obtaining the maximum values for the 2D material and Ref sample (1.64 and 1.62, respectively). The incorporation of the dendritic structures is expected to create more complex architectures with elevated defect concentrations. A lower I_D/I_G ratio is found in 1D and 3D samples (1.51 and 1.50, respectively), suggesting a slighter short-range order. In contrast, the maximum I_D/I_G ratio in the 2D material denotes the obtaining of a higher defective structure. D* and D″ bands are evident, manifesting the occurrence of heteroatoms and topological defects into the carbonaceous structures [35].

Nevertheless, it is important to emphasize that defect concentrations in these carbon derived materials is also associated by the aggressive etching process used during their synthesis, which result in the obtaining of diverse porous structures formed by the selective removal of Si—C and Si—O bonds, giving as a result the presence of dangling and broken bonds in the highly amorphous carbon resulting materials [36]. Therefore, the Raman analysis illustrates that varying the complexity and branching of the dendrons may produce different degrees of defect accumulation. Such structural defects can become active reaction centres when exposed to NO_2 and can drastically change the performance of the sensor device [13].

To determine the impact of nitrogen incorporation from the dendritic structures (D1, D2, and D3) on the electronic properties, surface analyses are carried out by X-ray photoelectron spectroscopy (XPS). Full-survey spectra with the different electronic core levels (C1s, O1s, N1s, Si2p, Cl2p) and the Auger bands are displayed in Fig. S4 (supplementary information). Surface elemental composition (Table S4) indicates that the materials are mainly carbon-based (≈ 90 wt%) in the Ref, 1D and 3D samples, with slight variations in the 2D material (72 w%). This latter sample also reveals a higher O concentration (> 12 wt%), along with a 9

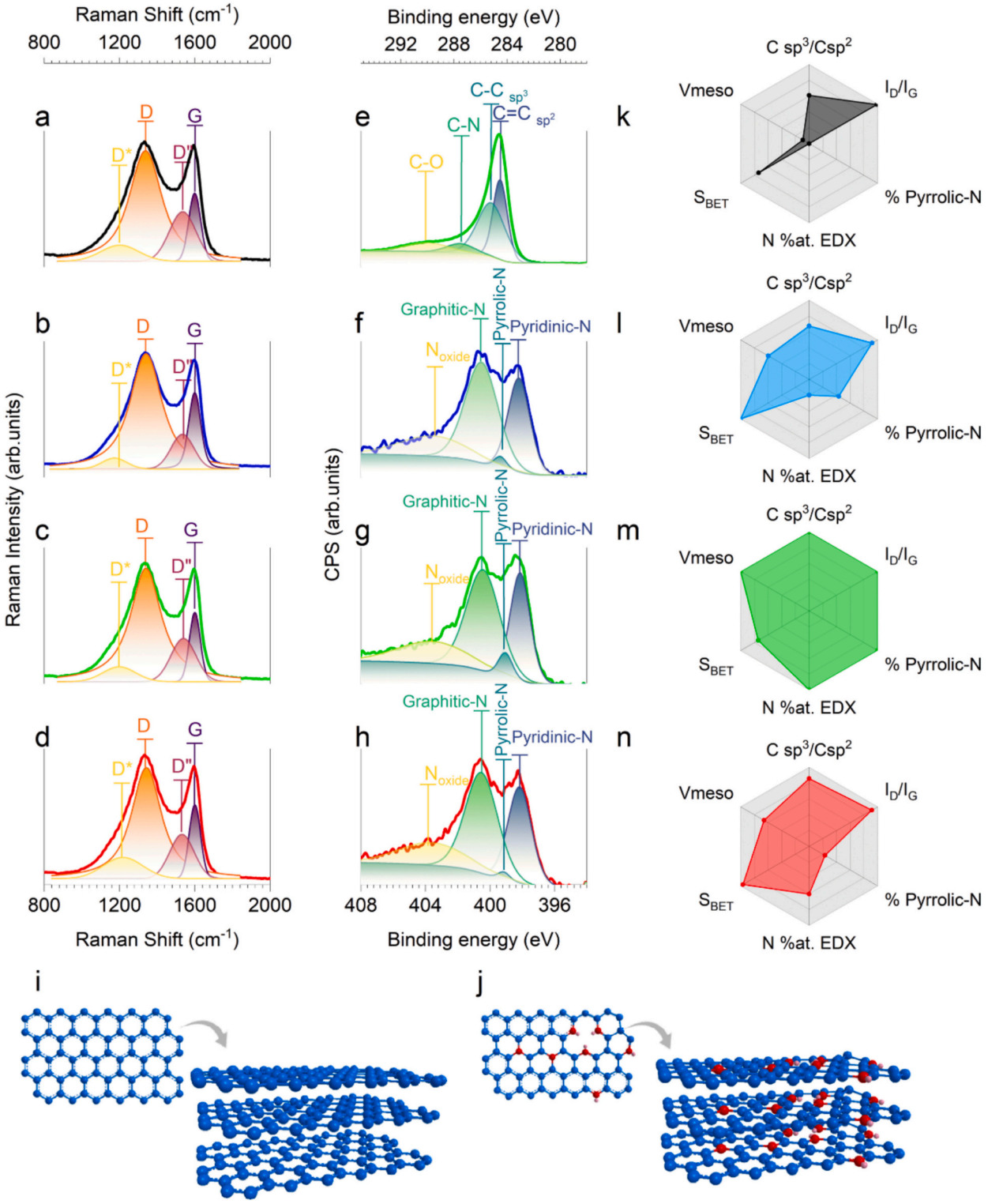

Fig. 2. Spectroscopic analysis, molecular modelling, and property mapping. Raman spectra and their corresponding Voigt curve fittings of the prepared materials a. Ref, b. 1D, c. 2D, and d. 3D samples. High-resolution and Gaussian peaks C1s-XPS spectrum of e. 2D sample and N1s-XPS spectra for f. 1D, g. 2D, and h. 3D samples. Representative simulated molecular structures of i. Ref sample, and j. N-doped samples (1D, 2D and 3D materials). Radar diagrams including the characteristic properties of the as-synthesized materials k. Ref, l. 1D, m. 2D, and n. 3D samples.

wt% of Si, retained after etching. In contrast, the Ref, 1D, and 3D materials exhibit lower oxygen levels, and only the 3D sample contains some traces of Si (< 1 wt%). Thus, in the 2D material, the oxygen concentration may be partially linked to the silicon, in the form of SiO_xC_{4-x} phases, while some oxygen comes from a slight oxidation surface bonded to the carbonaceous structure or to nitrogen species (Fig. S5e-h). The remaining silicon in the 2D sample may contribute to the higher defect concentration, which disrupts the carbon lattice [37]. Moreover, a N concentration above 5 wt% is detected for the N-doped samples, reaching a slightly higher content in the 2D material (5.6 wt%).

This result was previously corroborated by the elemental mappings acquired via EDS-TEM (Fig. 1g).

In Fig. 2e, the high-resolution C1s-XPS spectrum of the 2D sample is displayed as a representative example, and the rest of the C1s spectra are included in the Supplementary Information (Fig. S5a-d). The C1s are deconvoluted with Gaussian bands related to C-sp^2, C-sp^3, C—N (absence in Ref sample), C—O and a satellite peak (π- π* transition) [38,39]. The peak position, full width at half maximum (FWHM), area, and area-based peak proportions (% Conc.) are listed in Table S5. The most intense peaks centered at 284.6 and 285.3 eV correspond to C-sp^2 and C-sp^3, respectively. Specifically, the C-sp^3 contribution is associated with lattice distortions, reflecting the presence of structural defects [34]. Consequently, the ratio between both hybridization states Csp^3/Csp^2, is used to evaluate the disorder degree of the different carbonaceous structures. The ratio shows higher defect concentration in the N-doped materials (1D, 2D, and 3D) compared to the Ref sample (Table S5), highlighting the influence of the dendritic structures on the defect formation during synthesis. Among N-doped samples, the 2D sample exhibits the highest Csp^3/Csp^2 ratio, emphasizing its highly defective nature. The result is consistent with the Raman analysis, where superior I_D/I_G ratio is also obtained (Table S3).

The peak related to π- π* transition is distinguished in the prepared materials, highlighting the existence of a π-conjugated system. The π-system represents the electron delocalization in carbon materials, which translates into regions of high electron density [40]. Nitrogen doping influences the electronic properties of carbon materials, and can produce changes to the band related to π- π* transition. The 2D sample exhibits the largest relative concentrations of this band, followed by Ref, 1D and 3D samples, respectively (Table S5). The enhanced intensity of this satellite peak observed in the 2D sample, suggests a more efficient electronic transition π- π* which could be in favour to the sensing performance. Notably, in the 3D sample, it is observed a shift of this band which usually appears around 291 eV [41], to higher binding energies (Table S5), suggesting significant alterations in its electronic properties, a phenomenon that will be studied in the next section through the photoluminescence (PL) spectroscopy.

The nitrogen bonding configurations are investigated through the deconvolution of the high-resolution N1s XPS spectra of 1D, 2D and 3D materials (Fig. 2f-h). Data obtained from the deconvolution, including the relative concentrations of the nitrogen functionalities are collected in Table S5. The spectra suggest that nitrogen is fundamentally presented as graphitic-N (400.5 eV), pyridinic-N (398.2 eV) and N-oxide (403.5 eV) configurations [39], with relative concentrations exceeding 45, 29 and 20 %, respectively. A lower concentration of pyrrolic-N (399.0 eV) is also detected in all materials, showing notable variations for the 2D sample.

According to the literature, graphitic-N configurations are bonded to three adjacent C atoms in a hexagonal ring [20]. Pyridinic-N is bonded to two carbon atoms in hexagonal rings and pyrrolic-N is bonded in a five-membered heterocycle ring [37]. Therefore, in terms of defect contributions, pyridinic and pyrrolic nitrogens induce the formation of defects in the carbon lattice structure. Pyridinic-N is typically found at the edges or associated with vacancies, while pyrrolic-N, disrupts the lattice structure as a pentagonal ring. This is in good agreement with the above results, where a slightly higher relative concentration of pyrrolic-N is detected in the 2D sample, which correlates with its increased defect concentration compared to the 1D and 3D materials.

By way of illustration, Fig. 2i and Fig. 2j displayed a simulated molecular structure of the Ref sample, and a N-doped material. As represented, planar CDC structures are developed, where nitrogen atoms are disposed in the 1D, 2D and 3D materials in varied functionalities by the doping promoted by the different dendrons. This results in the obtaining of different structural parameters, as summarized in Fig. 2k-n. This figure represents hexagonal radar plots illustrating the most important structural parameters of the as-synthesized materials. Note that the values used for radar plotting are collected in Tables S1-S3 and S6. These include the I_D/I_G and Csp^3/Csp^2 ratios, the porous structure (V_{meso} and S_{BET}), and the nitrogen doping influence (at.%. N by EDX and %. pyrrolic-N). The radar plot for the 2D material (Fig. 2m) highlights its highly defective structure, as evidenced by Raman spectroscopy and XPS techniques. It also shows an increased N concentration revealed by EDS and XPS techniques, accompanied by a higher proportion of pentagonal pyrrolic-N concentration in comparison with the rest of the samples. These structural differences may significantly influence the sensor response during NO_2 interactions.

2.2. Gas sensing performance

The performance of the different chemiresistive gas sensors (Fig. S6) prepared with Ref, 1D, 2D and 3D materials is investigated, starting with their sensing capability towards 1 ppm of NO_2 at RT. Fig. 3a displays the time-responses of all sensors under dark conditions, operating without photoactivation via UV radiation. As observed, Ref, 1D and 2D sensors respond to the exposure of NO_2, an oxidizer analyte, with a decrease in their electrical resistance. This behaviour is characteristic of p-type sensitive materials where the adsorbed analyte, being an electron-acceptor, draws electrons through charge transfer, as has been previously reported in other carbon-based gas sensors [4,42]. The effect is more pronounced in the 2D sample, reaching a higher response compared to Ref and D1 materials. In contrast, the D3 sensor does not exhibit any response against the target gas.

The increased response of the 2D sensor towards the Ref and 1D samples can be attributed firstly, to the nitrogen doping, and secondly, to the elevated concentration of defects detected by XPS and Raman spectroscopy. Moreover, the presence of a hierarchically porous structure with a large V_{meso}, can be linked to a higher concentration of active sites for NO_2 adsorption, again improving the sensitivity to NO_2 [4]. For the D3 sensitive material, besides the similar microstructure to the 1D sample in terms of porosity structure (mainly in the micropore range), S_{BET}, and nitrogen doping, the obtained sensing performance is quite different between these two materials. This behaviour could be attributed to the molecular architecture of the initial dendritic structures (dendrons D1 and D3), a phenomenon that would be investigated in the next section, by PL spectroscopy.

Given the enhanced response of the 2D gas sensor, this device is further examined under different conditions, to evaluate the influence of photoactivation towards different NO_2 concentrations with varied radiant fluxes. Fig. 3b presents the results of exposing the 2D sensor to a steady state under different exposure scenarios. Initially, the sensor is exposed to air or NO_2 (0.1, 0.5 and 1 ppm) for several hours to reach a saturated state. Once the signal plateaus, photoactivation is gradually increased to its maximum level and then progressively reduced until full darkness is achieved. Two cycles of UV exposure are measured to obtain comparative data, reaching up to UV-210 % (143 W/m^2). It is worth noting the different R_0 (base resistance) values achieved for each condition: in air, the 2D sensor's resistance stabilizes around 30 kΩ. However, in the presence of NO_2, R_0 decreases to approximately 21 kΩ at 0.1 ppm, 19 kΩ at 0.5 ppm, and 13 kΩ at 1 ppm.

In the first photoactivation cycle, the response of the 2D sensor shows three different processes. Initially, partial desorption of NO_2 occurs concurrently with carrier generation within the sample and enhanced exchange with NO_2, all of them facilitated by UV exposure. These processes suggest an optimal level of photoactivation, where molecule desorption and molecule-substrate charge transfer are simultaneously enhanced. As a result, key parameters such as sensitivity, recovery times, and saturation concentrations are positively impacted with a properly photoactivation. A crucial detail observed in the sensor response is that photoactivation prevents the sensor from being poisoned, enabling consistent behaviour over time. Therefore, significant resistance recovery is observed when the sensor operates under darkness conditions after photoactivation. The effect is attributed to the improved desorption of NO_2 molecules. Following this, a second

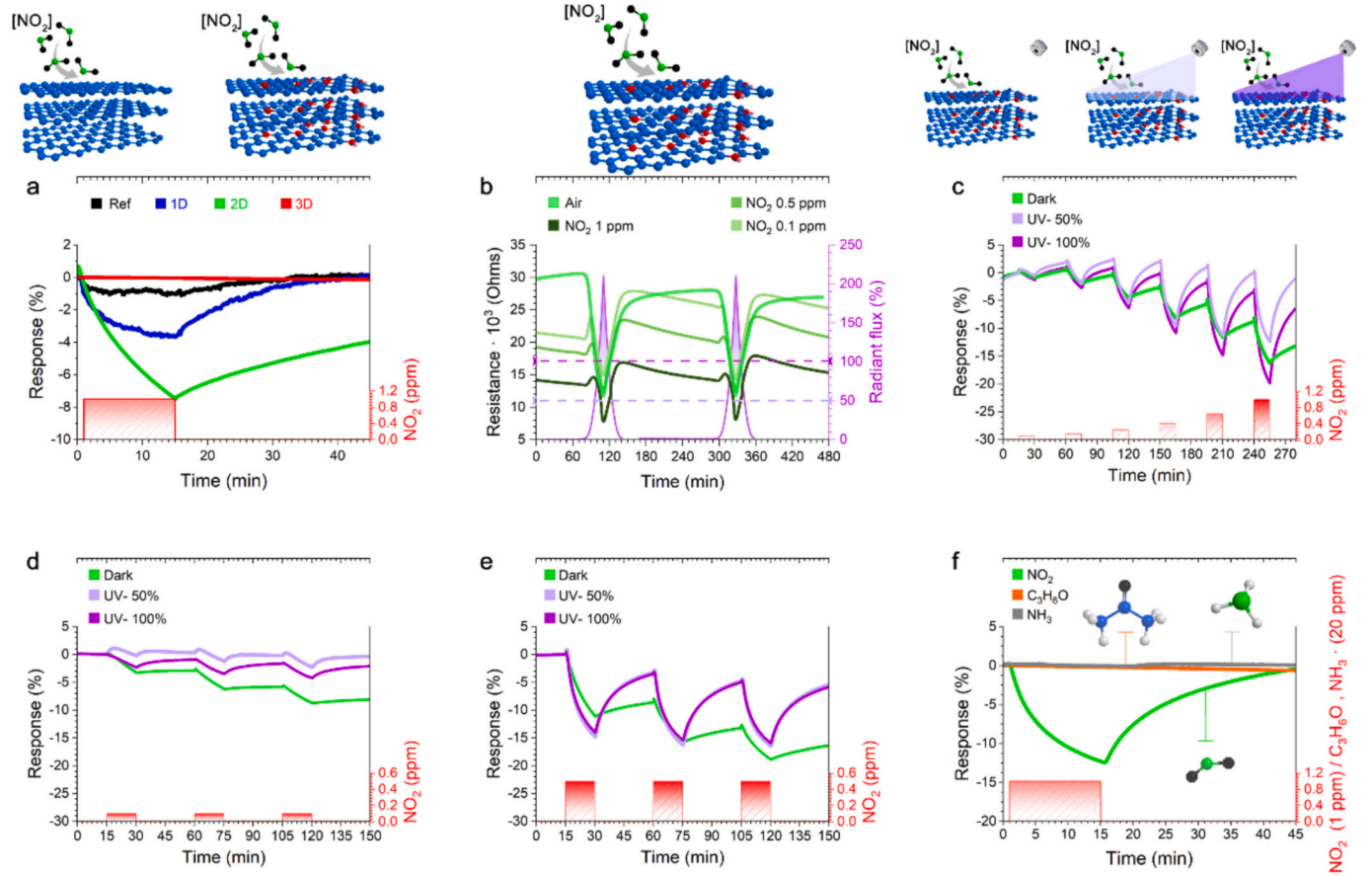

Fig. 3. Gas sensing performance of nitrogen-doped carbon materials towards NO_2 detection. a. Real-time response to 1 ppm of NO_2 without UV-light excitation of Ref sample (un-doped), 1D, 2D, and 3D materials (N-doped). b. The time-resistance curve of 2D sensor under different exposure conditions (air and 0.1, 0.5, and 1 ppm of NO_2). The two purple-shaded peaks represent the UV-light excitation carried out gradually increased up to 143 W/m^2. c. Calibration curve of the sensor build from 2D material at different NO_2 exposure concentrations (0.1, 0.15, 0.25, 0.40, 0.65 and 1 ppm) in the darkness, and photo activated under UV-50 % and UV-100 %. Time-dependent response of 2D sensor under dark conditions, UV-50 % and UV-100 % to d. 0.1 ppm NO_2, and e. 0.5 ppm NO_2. f. Target gas selectivity response of 2D sensor against 1 ppm of NO_2 and 20 ppm of acetone (C_3H_6O) and ammonia (NH_3).

prolonged exposure to NO_2 in darkness is conducted for 150 min, after a second photoactivation process. During this dark exposure, the sensor does not reach saturation at 0.1 ppm, but near-saturation state is obtained at higher concentrations of 0.5 ppm and 1 ppm. After the second photoactivation, the sensor's resistance returned to a level similar to those achieved after first photoactivation. This demonstrate the high resistance to be poisoned by interaction with NO_2 exposure or repeated photoactivation processes, without inducing degradation or permanent structural changes in the 2D sensor, ensuring long-term stability.

The sensing performance of the 2D sensor under photo-activation can be directly attributed to the designed microstructure. Regarding the effect of nitrogen doping, graphitic-N and pyridinic-N configurations play important roles in the sensing mechanisms, as both contribute with one electron to the aromatic π-system [43]. Pyridinic-N induces the electron distribution locally [37], exerting a smaller influence on the photoactivation response. In contrast, graphitic-N provides an extended contribution to the π-conjugation system, facilitating the electron delocalization and charge transfer, and making a significant enhancement to the sensing performance to NO_2 under photoactivation conditions [44]. Moreover, although pyrrolic-N is present in low concentrations, it contributes positively to sensing performance by adding two electrons to the π-system [43]. Its high reactivity, along with the substantial disruption promoted on the carbon lattice, induces the formation of active sites for NO_2 adsorption. Moreover, the mesoporous framework further complements these effects, ensuring fast interaction with target analytes [4,45,46].

Interestingly, the calibration curve shows that the D2 device exhibits a clear response to NO_2 concentrations as low as 0.1 ppm for exposure times of 15 min (Fig. 3c). In addition, it also highlights how UV exposure notably affects the sensing behaviour. Under dark conditions, a pronounced poisoning effect is observed, indicating incomplete desorption of the analyte after each exposure, particularly at higher concentrations. Upon irradiation, this effect is mitigated, demonstrating enhanced desorption capabilities. Optimizing photoactivation for specific concentrations is crucial due to the competitive processes of enhanced desorption and improved charge transfer. For concentrations below 0.5 ppm, UV-50 % displays better performance, evidenced by a steeper calibration curve slope. In contrast, the improvement at UV-100 % is clear at higher concentrations, as the calibration curve reaches a saturated or plateau state.

The limit of detection (LoD), defined as the lowest concentration of gas that sensor can reliably detect, can be calculated following Eq. (1) [47,48].

$$LoD_{(RMSnoise,Sensitivity)} = \frac{3*RMSnoise}{Sensitivity} \quad (1)$$

Where the sensitivity (% / ppm), is extracted from the calibration curve linear fit (Fig. S7) and the RMS noise is the root mean squared noise of the device signal during blank measurement. The RMS noise is multiplied by three in Eq. (1) to ensure the reliability of the LoD.

Photoactivation significantly enhances sensitivity because of improved recovery and charge exchange between NO_2 molecules and

the 2D-sensitive material. Under UV-50 % and UV-100 % conditions, the response reaches 28.9 ± 1.2 %/ppm and 26.8 ± 0.9 %/ppm, respectively (with fitting data obtained for concentrations below 0.5 ppm, prior to the saturation state). The LoD is approximately 1 ppb in both cases (UV-50 % higher than UV-100 %), with a noise level of 0.01 %. In dark conditions, a lower sensitivity of 14.5 ± 0.8 %/ppm is observed, with a LoD value around 2 ppb. However, under prolonged exposure, the LoD progressively increases with each subsequent exposure due to the lack recovery.

Furthermore, photoactivation also plays another important role in the sensing performance, by inducing the transition from p-type to n-type behaviour. This effect is observed in both nitrogen-doped materials; 2D and 1D as shown in Fig. 3d and Fig. S8, respectively. Notably, the 1D sample exhibits a more pronounced transition compared to the 2D material.

At low levels of photoactivation, the p-type behaviour of the samples is expected to invert to n-type due to the excitation of electrons into a high-energy electronic state introduced by the graphitic-N within the electronic structure. However, as the photoactivation power increases, the behaviour is anticipated to revert to p-type, as the effects of the graphitic-N are offset by the p-type doping contributions from the other nitrogen species.

The different sensing responses to NO_2 reached in 1D and 2D materials can be explained based on nitrogen doping that changes the electronic properties of the as-prepared materials. Considering that the reference exhibits p-type behaviour under different levels of photogeneration. Graphitic-N provides an n-type doping, by adding one valence electron to the electronic structure [49,50], while the other three nitrogen configurations (pyridinic-N, pyrrolic-N and N-oxide) induce p-type doping. This p-type doping is based on the electron deficiency in the π-system, attributed to the formation of these types of nitrogen functionalities close to vacancies [37,51].

Therefore, based on the relative concentrations of the varied nitrogen functionalities presented in Table S5, as well as the photoactivation power, sensitive materials could present either a n-type or p-type behaviour, as there are similar proportions of n-type and p-type related nitrogen bonds. However, a slightly increased proportion of graphitic-N was found in the 1D material (around 48 wt%), and therefore a predominant n-type response at photoactivation under UV-50 % can be tentatively attributed to this nitrogen bonding. It can be confirmed that this phenomenon is controllable by photoactivation power. Once the light power exceeds a specific threshold, the material transitions from exhibiting n-type to p-type sensor behaviour, keeping a high sensitivity to NO_2 (Fig. S8). This characteristic could offer a significant advantage in the future by enabling these sensors to function as multiparameter devices [52]. By modulating UV power, the sensors could be toggled between n-type and p-type behaviour, allowing the measurement of two distinct parameters with a single device and enhancing selectivity towards different target gases.

Fig. 3d-e illustrates the response of the 2D sensor to two sub-ppm NO_2 concentrations of 0.1 and 0.5 ppm, respectively. At 0.1 ppm (Fig. 3d), the 2D sensor exhibits a robust performance despite the poisoning effect, achieving mean values around 3.1 ± 0.3 %, 1.4 ± 1.1 %, and 2.6 ± 0.3 %, for dark, UV-50 %, and UV-100 % conditions, respectively. For 0.5 ppm (Fig. 3e), the poisoning effect is more pronounced in dark conditions, while UV irradiation conditions have a similar effect. The increase in the response can be related to improved desorption capabilities that free analyte adsorption sites, but also to improved adsorption mechanism, and charge transfer as evidenced but the slope and amplitude of the response during the first exposure. UV irradiation affects differently when the exposure is towards 0.5 ppm, providing mean responses of 7.9 ± 2.8 %, 13.2 ± 1.6 %, and 12.1 ± 1.6 % at dark, UV-50 %, and UV-100 % conditions, respectively. Thus, the mechanisms activated with UV previously commented; benefit the 2D sensor with up to 150 % increase on the mean response.

Noteworthy, UV exposure affects the device's base resistance. Under dark conditions, the resistance is around 28 kΩ, but it decreases to 24 and 18 kΩ for UV-50 % and UV-100 % conditions, respectively. This reduction can be explained by the effect of UV on the photogeneration of electron-hole pairs as the increased density of charge carriers may contribute to increased conductivity [53,54]. Besides, the unique ability of nitrogen doping in graphene and its derivatives is a key factor, as it effectively contributes electrons to the π-conjugated system. The effect is most noticeable in graphitic-N and pyrrolic-N configurations [55,56].

The selectivity of the 2D sensor is investigated by the exposure of the device to 20 ppm of acetone (C_3H_6O) and ammonia (NH_3), showing in Fig. 3f a comparison between the response behaviour to C_3H_6O and NH_3 vs NO_2. This plot (Fig. 3f), demonstrates the selectivity of the 2D sensor to NO_2, observing no significant changes in the electrical resistance upon exposure to either C_3H_6O or NH_3. Table 1 displays recent studies in the field of carbon-based materials for NO_2 sensing, including different carbon allotropes. Most of the studies including nitrogen-doping strategies are evaluated without UV photoexcitation, reaching limits of detections at the lowest of 500 ppb. However, the sensing performance of nitrogen-doped carbon sensors under photoexcitation remains unexplored. In this context, the 2D-sensitive material allows the detection of NO_2 in the sub-ppm level, reaching responses of 28.9 ± 1.2 %/ppm and 2.6 ± 0.3 % for 0.5 and 0.1 ppm respectively, under UV photoexcitation. In this work, we demonstrate that the unique combinations of mesoporosity, large defect concentration and effective nitrogen doping allow the obtaining of ultra-high sensitivity to NO_2 and LoD as low as 1 ppb, avoiding the poisoning effect by the photoexcitation.

2.3. *Optical properties: A UV–vis absorption and photoluminescence study*

To gain deeper insights into the optical properties and the electronic mechanisms involved, the designed samples are examined through UV–Vis and PL spectroscopies, to obtain the absorption spectra and the PL response at $\lambda_{exc} = 275$ nm, respectively. Fig. 4 shows the absorption and PL spectra of the prepared materials, alongside the optimized geometries of the dendritic molecules performed by a general MM+ Amber force field (GAFF).

In general terms, PL spectra provide valuable information about effective electron-hole radiative recombination processes, offering insights into the defect density, which can trap charge carriers to promote the recombination phenomena [65]. The luminescence of carbon-derived structures can be mainly associated with defect/surface and subdomain state within the sp^2- carbon core [66]. Specifically, N-doping can modulate the optical features and their response depends on how nitrogen atoms are incorporated in the carbon core, enhancing the radiation transition probability [66,67], or creating mid-states that unveil non-fluorescence [68]. For instance, nitrogen-doping introduces specific defect states that can modulate the PL response [69].

The absorption spectra of the prepared materials are shown in Fig. 4a. Starting with the Ref sample, two distinct regions can be identified in the spectrum. The first region, below 310 nm and characterized by two different bands, and the second one composed by a very broad absorption at higher wavelengths. The high intensity peak located at 275 nm is characteristic to the $\pi \rightarrow \pi^*$ transition of the graphitic core (C═C or C—C) of sp^2 domains present in the sp^3 environment (region marked in green colour in the Fig. 4a) [70]. In contrast, the broad absorption band positioned at around 400 nm (region marked in blue colour in the Fig. 4a), suggest the contribution of different features that are overlapped, and may be assigned with $n \rightarrow \pi^*$ transitions of functional groups (primarily oxygen in the Ref material), and surface states containing electron lone pairs (i.e. electrons that remain unbonded to another atom) [71].

Transitioning to the N-doped materials, the different contributions of the broad band are more visible and can be linked to the nitrogen doping incorporated into the structures, as well as the high defect density promoted in the samples, as revealed in Fig. 2. Moreover, a distinct

Table 1
Sensing performance of varied carbon-based material (doped and un-doped).

Sensing Material	Doping element	T (°C)	Gas sensing / Concentration	Response	LoD	UV radiation	Ref
Cg-C_3N_4	N (Grph)	200 °C	NO_2/50 ppm	71.26 %	7.39 ppm	–	[57]
MWCNT	N	RT	NO_2/5 ppm	24.82 %	<0.25 ppm	–	[58]
SWCNT	N (Pyd/Pyr)	RT	NO_2/10 ppm	27.70 %	500 ppb	–	[59]
Graphene g-C_3N_4	N (Grph)	RT	NO_2/5 ppm	21 %	600 ppb	–	[60]
Graphene	N (Pyr)	RT	NO_2/10 ppm	7.74 %	1 ppm	–	[61]
Graphene	Ag NWs	RT	NO_2/5 ppm	40 %	–	365 nm	[62]
Graphene	–	RT	NO_2/100 ppm	26 %	42.18 ppb	265 nm	[63]
Graphene	–	RT	NO_2/1 ppm	25 %	–	370 nm	[64]
FLMG	–	RT	NO_2/0.5 ppm	16 %	25 ppb	275 nm	[4]
This work	N (Grph/Pyd)	RT	NO_2/0.5 ppm	13.2 %	1 ppb	275 nm	
			NO_2/0.1 ppm	2.6 %			

SWCNT: single-walled carbon nanotube, MWCNT: multi-walled carbon nanotube, FLMG: few-layered mesoporous graphene. Grph: graphitic-N, Pyd: pyridinic-N, Pyr: pyrrolic-N.

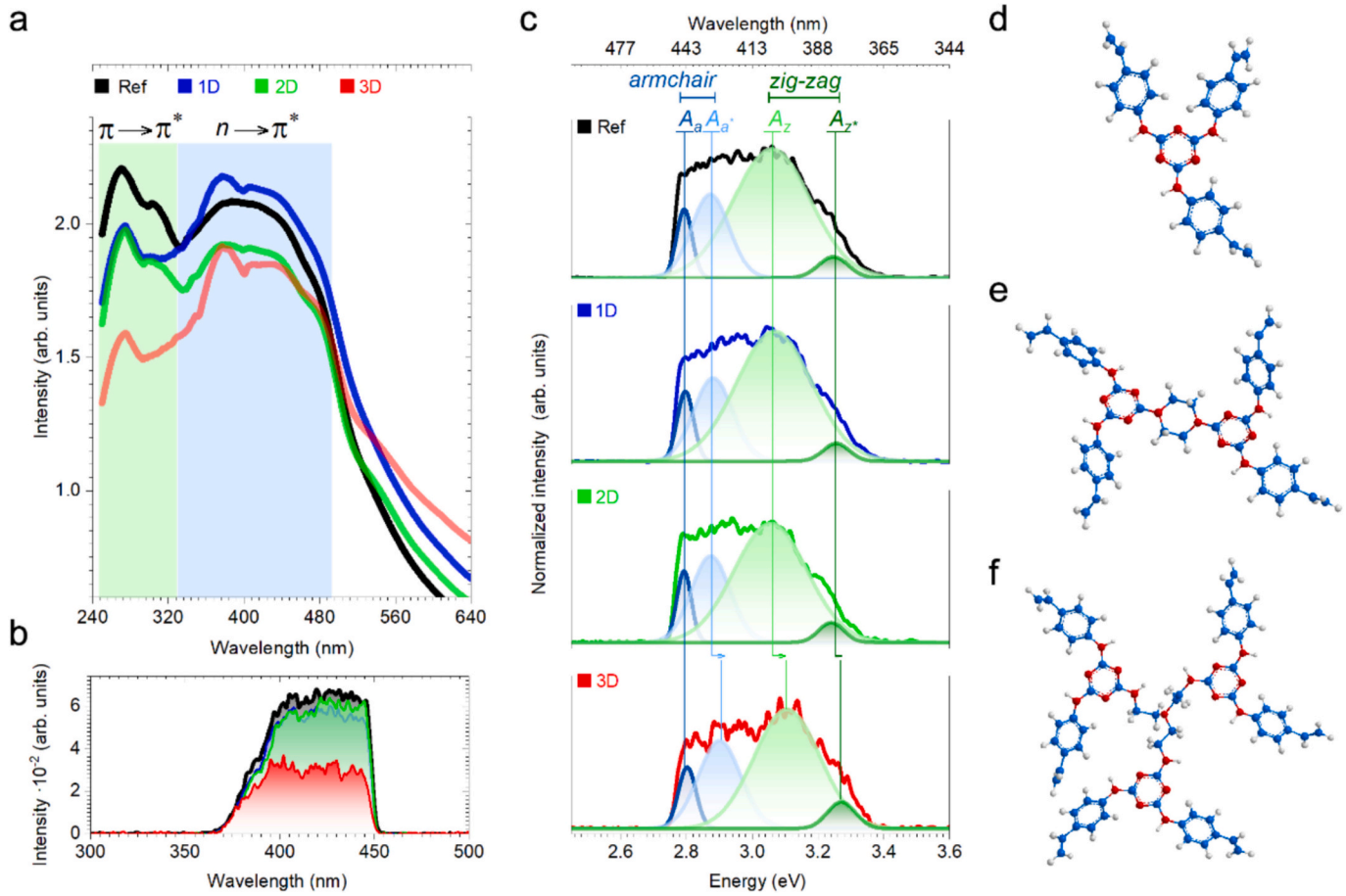

Fig. 4. Optical properties and their influence on the molecular geometry of nitrogen-doped CDC materials. Optical properties investigations of Ref, 1D, 2D and 3D materials studied from the a. absorption spectra (UV–Vis spectroscopy) b. emission PL spectra obtained at excitation wavelength of 275 nm, and c. curve-fitting of the PL spectra presented in b. Molecular geometries obtained from the minimization of energy by general MM+ Amber force field (GAFF) of the different dendritic structures d. D1, e. D2, and f. D3.

feature is clearly distinguished in this less energetic region with the presence of a new peak positioned at 377 nm, which is more notable in the 3D sample, followed by 1D and 2D materials (Fig. 4a). The heightened intensity of this peak is evident in the 3D and 1D materials, and is such that it surpasses the band located at 275 nm, suggesting a loss of efficiency in promoting the π → π * transitions (Fig. 4a). This can be related to the shift of the π- π* transition band discerned in the 1D and 3D-related C1s-XPS spectra (Table S5), suggesting an alteration into the π-cloud, that can be attributed to a reduction in the electron delocalization, which hinders the electron-hole recombination process. In contrast, in the 2D materials' spectrum, similar intensities are observed in both regions, suggesting a suitable proportion of π → π * and n → π * transitions, resulting in an improvement of the sensing performance.

Fig. 4b collects the PL spectra of Ref, 1D, 2D and 3D materials at the excitation wavelength of 275 nm, one of the main absorption bands observed in Fig. 4a. 1D and 2D samples show similar emission spectra to the Ref, in contrast to the lower emission observed in the 3D material (Fig. 4b). To delve deeper in this phenomenon, a curve fitting of these emission spectra is performed to correlate the microstructure and the photoluminescence properties. The spectra are converted to the energy

scale (eV) via the Jacobian transformation [72], ensuring good reliability of data and the applied fittings. As can be seen in Fig. 4c, the PL spectra present a broadband constituted by different features between 468 nm (2.64 eV) and 365 nm (3.39 eV). During the analysis, it is found that four Gaussian functions fitted very well all PL spectra, including the information obtained from the curve fitting in Table S7. Bands peaking at 3.24 eV (382 nm) and 3.06 eV (406 nm) can be attributed to $\pi \rightarrow \pi^*$ transitions for C═C of sp^2 domain in zigzag configuration, while the bands centered at 2.88 eV (431 nm) and 2.79 eV (444 nm) can be assigned to armchair configurations [73]. No relevant variations in the positions or the intensities of the different bands are observed in the 1D, 2D and Ref samples (Table S7), denoting that these microstructures lead to similar photoluminescence performance. In contrast, a slight blue shift of the most intensity bands (3.24, 3.06 and 2.88 eV) is elucidated from the curve fitting of the 3D sample, suggesting a distinct microstructure.

To evaluate the contribution of both edges (armchair vs zigzag), a ratio between the areas of the most intensity bands representing the armchair and zigzag edges (A_{a^*}/A_z); i.e. bands peaking at 2.88 and 3.06 eV respectively, is calculated (Table S7). The obtained A_{a^*}/A_z for the N-doped samples are higher compared to the Ref material, strongly suggesting the increased formation of zigzag edges by the introduction of the dendritic structures, and reaching the maximum A_{a^*}/A_z value for the 3D sample. These differences can be tentatively linked with the initial dendritic structures used for nitrogen doping. Fig. 4d-f displays the molecular geometries of the dendrons, organized from top to bottom according to the molecular rigidity; i.e., dendron D1 exhibits the highest rigidity, while D2 and D3 present intermediate and lower rigidity, respectively. Based on the PL spectra and the information obtained from the curve fitting (Table S7), it can be stablished that the rigidity of the dendrons plays an important role in the promotion of armchair vs. zigzag edge. A higher concentration of armchair edges along with a quenching PL emission is obtained with the nitrogen doping promoted by the D3 dendritic structure. This can be correlated with the absence of response to 1 ppm of NO_2, showed in Fig. 3 by the 3D material. Thus, despite the similar N content (above 5 wt%,Table S4) introduced in the 3D sample compared to the other two N-doped materials, along with the large S_{BET} and defect concentrations revealed in Fig. 1, and Fig. 2, all these microstructural features seem to act as non-radiative active centers, quenching the PL emission [65].

This indicates that is crucial not only to synthesized highly porous defective microstructures and with nitrogen heteroatoms to reach ultrasensitive NO_2 devices, but also to do it effectively. To create abundant and accessible trap sites is essential, as these sites participate in interaction with the NO_2 molecules, and play a key role in the redox reactions that drive the sensing performance. Consequently, tailoring the molecular architecture is crucial to reach a good sensing performance to NO_2, and the novel dendritic structures employed for the nitrogen doping highly affects the final CDCs microstructures. This aligns with the investigation conducted by Blum et al. [74], revealing that ceramic structures obtained from the thermal treatment of PDCs, present the ability to "memorize" the initial polymer architecture, affecting the final properties of the materials, and highlighting the importance on the initial architecture of the starting polymer. Therefore, our initial dendritic structures which polymerize within the AHPCS, govern the final CDC structures, leading to different sensing performances.

3. Conclusion

We report the synthesis of nitrogen-doped carbide-derived carbon materials using a polymer-derived ceramic route and dendritic molecular architectures specifically engineered to modulate porosity, defect density, and nitrogen incorporation. The use of tailored D2 dendron facilitates the formation of highly disordered carbon networks, enabling the effective integration of nitrogen heteroatoms predominantly as graphitic-N and pyridinic-N species. These structural features play a central role in gas adsorption and charge transport, resulting in enhanced interaction with nitrogen dioxide molecules. Notably, the 2D-sensitive material achieves outstanding sensing performance at room temperature, detecting NO_2 concentrations as low as 1 ppb under UV illumination and showing a 13.2 % response at 0.5 ppm. This represents a significant step forward in carbon-based gas sensing, where achieving high sensitivity at ambient conditions remains a key challenge. The synergistic effect of controlled nitrogen doping and hierarchical porous architectures leads to a strong enhancement of the π-conjugated electronic structure, directly impacting sensor performance. Our results underscore the potential of molecular-level design strategies to control the structural and electronic properties of carbon-based sensing materials. This approach opens new directions for the rational design of functional materials for room-temperature gas sensing, with implications in environmental monitoring, health diagnostics, and smart sensing technologies.

4. Experimental section

4.1. Preparation of the dendritic structures

Three different nitrogen-containing dendrons (D1, D2 and D3) are prepared by varied substitution reactions under controlled temperature synthesis. The dendritic structure D1 is synthesized according to the method reported previously [24]. Then, D2 and D3 molecules are prepared from an organic molecule obtained from the di-substitution (D1-d) of the cyanuric chloride involved in the preparation of D1 dendron.

The synthesis of D1-d and the obtention of D2 and D3 dendrons are described as follows:

All the reactants involved in the chemical reactions were used in their as-received state without further purification, and reactions were monitored by thin layer chromatography (TLC) using F_{254} aluminium oxide coated plates. Purification of the final products was performed by column chromatography, employing silica gel 60 (60–120 mesh) from Merck (USA) as the stationary phase, and using the suitable solvent for each dendritic structure.

i) Di-substituted molecule (D1-d): 6-chloro-N^2, N^4-bis (4-vinyl phenyl)-1,3,5-triazine-2,4-diamine

In a flask, (16 g, 0.086 mol) of cyanuric chloride ($C_3N_3Cl_3$) and (35 mL, 0.2 mol) of DIPEA (N, N-diisopropylethylamine), both from Sigma Aldrich (USA), were dissolved in (250 mL) of anhydrous tetrahydrofuran (THF). The mixture was stirred at RT and purged with argon to obtain an inert atmosphere. Once a homogenous dissolution was achieved, (30.18 mL, 0.258 mol) of 4-vinylaniline (90 %) from Fisher Scientific (USA) was added dropwise, followed by heating the mixture under reflux for 8 h. The obtained residue was purified by column chromatography using ethyl acetate/hexane (1:4) as eluent, obtaining a whitish solid product (> 85 % yield).

ii) Dendron D2: 6,6′-(piperazine-1,4-diyl) bis (N^2, N^4-bis (4-vinyl phenyl)-1,3,5-triazine-2,4-diamine

D2 was prepared by mixing (4 mL, 0.023 mol) of DIPEA and (688 mg, 0.008 mol) of piperazine (Sigma Aldrich, USA) in (250 mL) of anhydrous THF. Then, (5.5 g; 0.016 mol) of D1-d molecule was dissolved in anhydrous THF and incorporated to the previous mixture. The reaction was stirred, bubbled with argon and sealed in a Parr's vessel to ensure non-oxygen contamination, and heating at 80 °C for 12 h. The final product was obtained by column chromatography with dichloromethane /methanol (5:1) as eluent to obtain a white product (> 85 % yield).

iii) Dendron D3: N^2-(2-(bis(2-((4,6-bis((4-vinyl phenyl)amino)-1,3,5-triazine-2-yl)amino)ethyl)-N^4,N^6-bis(4-vinyl phenyl)-1,3,5-triazine-2,4,6-triamine

A dissolution of (6.95 mL, 0.04 mol) of DIPEA and (1.168 g, 0.008 mol) of Tris(2-aminoethyl) amine (Sigma Aldrich, USA) was prepared in 250 mL of anhydrous THF. Then, (10 g, 0.028 mol) of D1-d molecule was dissolved in anhydrous THF and incorporated into the previous solution, obtaining a mixture that was stirred, bubbled in argon and sealed in a Parr's vessel to remove the oxygen content. Then, the mixture was heated at 80 °C for 14 h until the consumption of the D1-d molecule was detected by TLC. Once chemical reaction was completed, the solvent was removed by using a rotatory evaporator, and the final residue was obtained by washing the solid with ethyl acetate and acetone, obtaining a yellowish solid (6 g, > 90 % yield).

The characterization of the novel dendritic molecules is collected in the supplementary information, section S3.

4.2. Highly porous nitrogen-doped CDC material preparation

Three different nitrogen-doped CDC samples were prepared by individually mixing a liquid commercial allyl-hydrido polycarbosilane (AHPCS, SMP-10®, Starfire Systems, USA) with the prepared dendritic structures (D1, D2 and D3) in anhydrous THF. The mixtures were performed on a Schlenk line, under an argon atmosphere. The AHPCS and the corresponding dendrons were mixed in a 90/10 wt/wt ratio respectively, in the presence of a 1 wt% of platinum catalyst (Platinum-1,3-divinyl-1,1,3,3-tetramethyldisiloxane (3–3.5 %Pt, abcr GmbH, Germany). The mixtures were intensively stirred under Ar for 48 h. After completion of the reactions, solvent removal was carried out by a rotatory evaporator, and samples were subjected to a thermal treatment in an alumina tubular furnace to produce the polymer-to-ceramic transformation. Materials were heated to 280 °C for 5 h, followed by a ramp to 700 °C for 2 h, with a controlled heating rate of 5 °C/min under a continuous argon flow of 150 mL/min. The resulting materials were ground in an agate mortar and sieved below 45 um prior to the subsequent chemical etching. Samples underwent selective etching through chlorination treatment, in a quartz tubular furnace. Chlorination was conducted at the same temperature as in pyrolysis treatment (700 °C) for 2 h, with a continuous Cl_2/N_2 flow of 25 mL/50 mL, respectively. Heating and cooling of the samples were performed in an N_2 atmosphere with a flow rate of 100 mL/min and a fixed heating rate of 5 °C/min. Finally, samples were subjected to further thermal treatment to remove the trapped chlorine traces, heating the materials until 500 °C for 4 h with a continuous N_2/H_2 flow. Materials were finally subjected to milling and sieving below 50 um.

Four different samples were evaluated during this study, three N-doped CDC materials prepared with the different dendrons, and labelled as 1D, 2D, and 3D, representing the samples prepared from each dendritic structure; D1, D2 and D3 dendrons respectively, and a reference material without nitrogen doping. This latter sample was obtained by subjecting the commercial AHPCS to the same pyrolysis and chlorination thermal treatments described previously. The reference material was labelled as Ref.

4.3. N-doped CDC characterization

The prepared CDC materials were studied through XPS technique (SPECS GmbH, Germany) to corroborate the nitrogen incorporation and their bonding configuration into the final structures. XPS were performed in an instrument equipped with a PHOIBOS 150 9MCD as an energy analyser and monochromatic Mg was employed as an energy source. Curves were deconvoluted through CASA© software using the Shirley background. Raman characterization was employed to assess the carbonaceous structure, focusing on the evaluation of the defects present in the materials. Raman spectra were acquired from a confocal Raman microscope WITec ALPHA 300RA (Germany) (Nd:YAG laser light source of 532 nm in p-polarization), showing average spectra from representative regions. Spectral analysis was conducted in the spectral range of 65–3850 cm^{-1}, using a 600-g/mm grating with a spectral resolution of 0.2 cm^{-1}. To avoid sample damage and overheating effects during measurements, an objective with a numerical aperture of 0.95 and a laser output power of 0.7 mW were used.

Textural characterization was performed to evaluate the porosity network and the corresponding S_{BET} created after chlorination treatment, by the N_2 adsorption-desorption technique (Tristar, Micromeritics, USA). Samples were degassed at 120 °C for 18 h and data calculations were performed by Brunauer-Emmet-Teller (BET) and Barrett-Joyner-Halenda (BJH) methods [75,76] to estimate the S_{BET} and pore size distribution, respectively. The order arrangement of the porous structure was evaluated by XRD, performing the sample measurements employing a PANalytical X-ray diffractometer (Empyrean, United Kingdom) equipment with Cu-K_α ($\lambda \sim 1.5406$ Å) radiation.

The microstructural parameters of the CDC samples were studied by transmission electron microscopy (TEM), high-resolution transmission electron microscopy (HRTEM), scanning transmission electron microscopy (STEM) and X-ray energy dispersive spectroscopy (EDS) were conducted with a JEOL 2100 (Japan) field emission gun transmission electron microscope operating at 200 kV and equipped with an 80 X-MaxEDX spectrometer. Samples were prepared by placing aliquots of the desired material onto Cu grids supported by a lacey carbon film. Elemental mapping was performed via EDS to confirm the nitrogen doping content in the prepared materials.

The UV-absorption properties are evaluated by UV–Vis spectroscopy, using a Perkin Elmer (USA) Lambda 650 UV–Vis-NIR spectrophotometer equipped with an integrating sphere, and measuring the absorption spectra at RT.

The photoluminescence study was carried out by acquiring the emission spectra using a fluorescence spectrometer (FS5 from Edinburgh Instruments) equipped with a Xenon lamp of 150 W. Specifically, the excitation wavelength was fixed 275 nm with an excitation bandwidth of 5 nm, whereas the emission scan goes from 300 to 600 nm and the emission bandwidth was 1 nm.

The optimisation of the molecular rearrangement of the varied dendritic structures was carried out using GAFF Force Field in Avogadro (v 1.2.0).

4.4. Gas sensors fabrication

To study the potential chemiresistive sensing properties of the prepared CDC materials, the varied samples in powder form were first dispersed in *n*-methyl-2-pyrrolidone (NMP; Sigma Aldrich, USA) at a concentration of 1 mg/mL and sonicated in a bath until stable suspensions were obtained. Then, each solution was deposited using dielectrophoresis-assisted (10 kHz, 10 Vpp) drop-casting deposition onto an interdigitated electrode (IDE) substrate (DRP-G-IDEAU10, DropSens) to fabricate the different gas sensor devices.

As a representative example, Fig. S6c-d shows the optical micrograph in the dielectrophoresis-assisted drop-casting process resulting in the formation of aligned 2D nanoparticles in the form of chains, which contact both electrodes on the IDE substrate. Briefly, during the solvent evaporation process, an alternating electric field induces nanoparticle growth between the electrodes, continuing until sufficient contacts are established, allowing the passage of electrical current under the applied voltage. An electrical resistance of approximately 20 kΩ is obtained after deposition.

4.5. Evaluation of gas sensing performance

Each sensor was placed in a 3D-printed polylactic acid (PLA) airtight cell (with a volume of ≈ 10 mL) connected to an automated gas generator as depicted in Fig. S6a-b. The airflow inside the cell was

maintained at 50 mL/min. Measurements were carried out by exposing the sensor to a mixture of target gas cylinders of NO_2 (1 ppm), C_3H_6O and NH_3 (20 ppm) and synthetic dry air, which was used for purging.

All gases were supplied by Nippon Gases, Spain. Mass flow controllers were used to adjust the concentration of each gas sample through custom-made LabView software that simultaneously monitor the device's resistance with a digital multimeter (HP 34401 A, USA).

A 275 nm UV light-emitting diode (SeoulViosys CA3535 - CUD7GF1B) was placed inside the chamber and controlled with a DC source to irradiate the device during the sensing measurements at variable power densities (68 W/m^2 at 100 %). Percentages are given through the manuscript as UV- followed by its corresponding number.

To evaluate the sensing capabilities of the 2D material, three distinct experiments were conducted. First, an experiment was designed to study the adsorption and desorption mechanisms by exposing the sensor to variable UV irradiating intensity under analyte-saturated conditions, i.e., under constant exposure to analyte concentrations (0, 0.1, 0.5, and 1 ppm of NO_2). Second, a calibration curve was designed using cycles with the same exposure and recovery durations as in the constant concentration experiment and exposing the sensor to varying NO_2 concentrations (0.1, 0.15, 0.25, 0.40, 0.65, and 1 ppm).

The sensing performance evaluation collected in Fig. 3 is presented as the response of the device, defined as time-dependent change in the sensor's resistance when exposed to the gas according to Eq. (2):

$$Response(\%) = \left|\frac{\Delta R}{R_0} * 100\right| \quad (2)$$

Where R is the resistance of the device at each moment, and R_0 is the base resistance of the device, measured during baseline stabilization before the first exposure.

Finally, three consecutive exposures to a constant concentration of NO_2 (0.1 and 0.5 ppm) were performed. The experiment began with a baseline, followed by three cycles of 15-minute exposures to the analyte, with a 30-minute recovery phase, during which only the carrier gas was passed through the device.

CRediT authorship contribution statement

Berta Pérez-Román: Writing – original draft, Investigation, Formal analysis, Data curation. **Jesús López-Sánchez:** Writing – review & editing, Methodology, Investigation, Conceptualization. **M. Alejandra Mazo:** Writing – review & editing, Supervision, Conceptualization. **Álvaro Peña:** Writing – review & editing, Investigation, Formal analysis, Data curation. **David G. Calatayud:** Investigation. **Pilar Marín:** Funding acquisition. **Laura Pascual:** Writing – review & editing, Investigation. **Rocío E. Rojas-Hernández:** Writing – review & editing, Investigation. **Daniel Matatagui:** Writing – review & editing, Methodology, Investigation, Formal analysis, Conceptualization. **Fernando Rubio-Marcos:** Writing – review & editing, Validation, Supervision, Methodology, Funding acquisition, Formal analysis, Conceptualization.

Declaration of competing interest

The authors declare that they have no known competing financial interests or personal relationships that could have appeared to influence the work reported in this paper.

Acknowledgements

The authors acknowledge funding support from projects PID2023-153398OB-I00, PID2023-151036OA-I00, PDC2022-133039-I00, PID2021-123112OB-C21, TED2021-132800B-I00, and TED2021-129688B-C21 funded by MCIU/AEI/10.13039/501100011033 and the European Social Fund Plus (ESF+). P. M. acknowledges financial support from the Comunidad de Madrid through grant S2018/NMT-4321. R. E. R-H. is gratefully for financial support through the Estonian Research Council grant PSG-466. J. L.-S. acknowledges the financial support from grant RYC2022-035912-I funded by MCIU/AEI/10.13039/501100011033 and by the European Social Fund Plus (ESF+). D. M extents gratitude to financial support within the RYC2021-031166-I funded by MCIU/AEI/10.13039/501100011033 and by the European Social Fund Plus (ESF+). F. R-M. also expresses gratitude to Comunidad de Madrid for financial support through the Industrial Doctorates project (IND2020/IND-17375), co-financed by the European Social Fund. A. P. is gratefully to MCIN, for the funding from grant PRE2019-0875001234.

Appendix A. Supplementary data

Supplementary data to this article can be found online at https://doi.org/10.1016/j.cej.2025.167301.

Data availability

Data will be made available on request.

References

[1] K. Newell, C. Kartsonaki, K.B.H. Lam, O.P. Kurmi, Cardiorespiratory health effects of particulate ambient air pollution exposure in low-income and middle-income countries: a systematic review and meta-analysis, The Lancet Planetary Health 1 (2017) e368–e380, https://doi.org/10.1016/S2542-5196(17)30166-3.
[2] P. Orellano, J. Reynoso, N. Quaranta, A. Bardach, A. Ciapponi, Short-term exposure to particulate matter (PM10 and PM2.5), nitrogen dioxide (NO2), and ozone (O3) and all-cause and cause-specific mortality: systematic review and meta-analysis, Environ. Int. 142 (2020) 105876, https://doi.org/10.1016/j.envint.2020.105876.
[3] World Health Organization, WHO Global Air Quality Guidelines. Particulate Matter (PM2.5 and PM10), Ozone, Nitrogen Dioxide, Sulfur Dioxide and Carbon Monoxide, Geneva, 2021.
[4] D. Matatagui, J. López-Sánchez, A. Peña, A. Serrano, A. del Campo, O.R. de la Fuente, N. Carmona, E. Navarro, P. Marín, M. del Carmen Horrillo, Ultrasensitive NO2 gas sensor with insignificant NH3-interference based on a few-layered mesoporous graphene, Sensors Actuators B Chem. 335 (2021) 129657, https://doi.org/10.1016/j.snb.2021.129657.
[5] V.S. Bhati, M. Kumar, R. Banerjee, Gas sensing performance of 2D nanomaterials/metal oxide nanocomposites: a review, J. Mater. Chem. C 9 (2021) 8776, https://doi.org/10.1039/d1tc01857d.
[6] M. Chae, I.G. Kwon, D. Lee, H.D. Kim, Threshold trigger embedded gas sensor for low-power and real-time atmospheric NO2 monitoring using drones, Chem. Eng. J. 507 (2025) 160605, https://doi.org/10.1016/j.cej.2025.160605.
[7] Y. Yang, M. Zhu, H. Zhang, B. Wang, C. Chen, J. Li, Y. Wang, J. Hao, Room temperature gas sensor based on rGO/Bi2S3 heterostructures for ultrasensitive and rapid NO2 detection, Chem. Eng. J. 490 (2024) 151872, https://doi.org/10.1016/j.cej.2024.151872.
[8] C. Wang, L. Yin, L. Zhang, D. Xiang, R. Gao, Metal oxide gas sensors: sensitivity and influencing factors, Sensors 10 (2010) 2088–2106, https://doi.org/10.3390/s100302088.
[9] M. Šetka, M. Claros, O. Chmela, S. Vallejos, Photoactivated materials and sensors for NO2monitoring, J. Mater. Chem. C 9 (2021) 16804–16827, https://doi.org/10.1039/d1tc04247e.
[10] A. Mondal, P.V.K. Yadav, Y. Ashok Kumar Reddy, A review on device architecture engineering on various 2-D materials toward high-performance photodetectors, Mater. Today Commun. 34 (2023) 105094, https://doi.org/10.1016/j.mtcomm.2022.105094.
[11] R. Kumar, X. Liu, J. Zhang, M. Kumar, Room-temperature gas sensors under photoactivation: from metal oxides to 2D materials, Nano-Micro Lett. 12 (2020), https://doi.org/10.1007/s40820-020-00503-4.
[12] Á. Peña, J. López-Sánchez, L. Sacco, S. Vollebregt, J. Marqués-Marchán, M. C. Horrillo, P. Marín, D. Matatagui, Beyond conventional characterization: defect engineering role for sensitivity and selectivity of room-temperature UV-assisted graphene-based NO_2 sensors, Talanta 286 (2025) 127507, https://doi.org/10.1016/j.talanta.2024.127507.
[13] Á. Peña, D. Matatagui, F. Ricciardella, L. Sacco, S. Vollebregt, D. Otero, J. López-Sánchez, P. Marín, M.C. Horrillo, Optimization of multilayer graphene-based gas sensors by ultraviolet photoactivation, Appl. Surf. Sci. 610 (2023) 155393, https://doi.org/10.1016/j.apsusc.2022.155393.
[14] P. Ivanov, E. Llobet, F. Blanco, A. Vergara, X. Vilanova, I. Gracia, C. Cané, X. Correig, On the effects of the materials and the noble metal additives to NO2 detection, Sensors Actuators B Chem. 118 (2006) 311–317, https://doi.org/10.1016/j.snb.2006.04.036.
[15] L.Y. Zhu, L.X. Ou, L.W. Mao, X.Y. Wu, Y.P. Liu, H.L. Lu, Advances in noble metal-decorated metal oxide nanomaterials for chemiresistive gas sensors: overview, Nano-Micro Lett. 15 (2023), https://doi.org/10.1007/s40820-023-01047-z.

[16] T. Miyamoto, J. Katagiri, K. Nagashima, M. Murakami, Effect of Ag addition on the mechanical properties of bulk superconductors, IEEE Trans. Appl. Supercond. 9 (1999) 2066–2069, https://doi.org/10.1109/77.784872.
[17] L. Zhu, J. Wang, J. Liu, M.S. Nasir, J. Zhu, S. Li, J. Liang, W. Yan, Smart formaldehyde detection enabled by metal organic framework-derived doped electrospun hollow nanofibers, Sensors Actuators B Chem. 326 (2021) 128819, https://doi.org/10.1016/j.snb.2020.128819.
[18] C. Doroftei, P.D. Popa, F. Iacomi, L. Leontie, The influence of Zn2+ ions on the microstructure, electrical and gas sensing properties of La0.8Pb0.2FeO3 perovskite, Sensors Actuators B Chem. 191 (2014) 239–245, https://doi.org/10.1016/j.snb.2013.09.113.
[19] S. Srivastava, P. Pal, D.K. Sharma, S. Kumar, T.D. Senguttuvan, B.K. Gupta, Ultrasensitive boron−nitrogen-Codoped CVD graphene-derived NO2 gas sensor, ACS Mater. Au 2 (2022) 356–366, https://doi.org/10.1021/acsmaterialsau.2c00003.
[20] A. Mirzaei, S.P. Bharath, J.Y. Kim, K.K. Pawar, H.W. Kim, S.S. Kim, N-doped graphene and its derivatives as resistive gas sensors: an overview, Chemosensors 11 (2023) 334, https://doi.org/10.3390/chemosensors11060334.
[21] Z. Wang, L. Zhu, J. Wang, R. Zhuang, P. Mu, J. Wang, W. Yan, Advances in functional guest materials for resistive gas sensors, RSC Adv. 12 (2022) 24614–24632, https://doi.org/10.1039/d2ra04063h.
[22] G. Yushin, A. Nikitin, Y. Gogotsi, Carbide-Derived Carbon, 2006, https://doi.org/10.1201/9781420004014.ch8.
[23] S. Ratso, I. Kruusenberg, M. Käärik, M. Kook, R. Saar, M. Pärs, J. Leis, K. Tammeveski, Highly efficient nitrogen-doped carbide-derived carbon materials for oxygen reduction reaction in alkaline media, Carbon N. Y. 113 (2017) 159–169, https://doi.org/10.1016/j.carbon.2016.11.037.
[24] B. Pérez-Román, A. Merchán del Real, J. Rubio, M.A. Mazo, F. Rubio-Marcos, Innovative strategies for nitrogen-incorporating silicon oxycarbide-based preceramic polymer synthesis, Mater. Adv. 5 (2024) 2040–2056, https://doi.org/10.1039/d3ma00898c.
[25] M. Thommes, K. Kaneko, A.V. Neimark, J.P. Olivier, F. Rodriguez-Reinoso, J. Rouquerol, K.S.W. Sing, Physisorption of gases, with special reference to the evaluation of surface area and pore size distribution (IUPAC Technical Report), Pure Appl. Chem. 87 (2015) 1051–1069, https://doi.org/10.1515/pac-2014-1117.
[26] S. Kaur, G. Mônego, K. Rezwan, M. Wilhelm, Synthesis of porous Ni/SiC(O)-based nanocomposites: effect of nickel acetylacetonate and poly(ethylene glycol) methacrylate modification on specific surface area and porosity, Adv. Eng. Mater. 22 (2020) 1901036, https://doi.org/10.1002/adem.201901036.
[27] B. Perez-Roman, R. Layek, M.A. Rodriguez, F. Rubio, J. Rubio, A. Tamayo, Insights into the structural and surface characteristics of microporous carbide derived carbons obtained through single and double halogen etching, Microporous Mesoporous Mater. 310 (2021) 110675, https://doi.org/10.1016/j.micromeso.2020.110675.
[28] D. Liqun, M. Qingsong, C. Zhaohui, Etching process of silicon oxycarbide from polysiloxane by chlorine, Corros. Sci. 94 (2015) 237–244, https://doi.org/10.1016/j.corsci.2015.02.004.
[29] Y. Ishii, Y. Nishiwaki, A. Al-Zubaidi, S. Kawasaki, Pore size determination in ordered mesoporous materials using powder X-ray diffraction, J. Phys. Chem. C 117 (2013) 18120–18130, https://doi.org/10.1021/jp4057362.
[30] A. Sadezky, H. Muckenhuber, H. Grothe, R. Niessner, U. Pöschl, Raman microspectroscopy of soot and related carbonaceous materials: spectral analysis and structural information, Carbon N. Y. 43 (2005) 1731–1742, https://doi.org/10.1016/j.carbon.2005.02.018.
[31] Z. Zafar, Z.H. Ni, X. Wu, Z.X. Shi, H.Y. Nan, J. Bai, L.T. Sun, Evolution of raman spectra in nitrogen doped graphene, Carbon N. Y. 61 (2013) 57–62, https://doi.org/10.1016/j.carbon.2013.04.065.
[32] J.H. Kaufman, S. Metin, D.D. Saperstein, Symmetry breaking in nitrogen-doped amorphous carbon: infrared observation of the Raman-active G and D bands, Phys. Rev. B 39 (1989) 13053–13060, https://doi.org/10.1103/PhysRevB.39.13053.
[33] M. Ayiania, E. Weiss-Hortala, M. Smith, J.S. McEwen, M. Garcia-Perez, Microstructural analysis of nitrogen-doped char by Raman spectroscopy: raman shift analysis from first principles, Carbon N. Y. 167 (2020) 559–574, https://doi.org/10.1016/j.carbon.2020.05.055.
[34] C. Zhang, W. Shen, K. Guo, M. Xiong, J. Zhang, X. Lu, A pentagonal defect-rich metal-free carbon electrocatalyst for boosting acidic O2Reduction to H2O2Production, J. Am. Chem. Soc. 145 (2023) 11589–11598, https://doi.org/10.1021/jacs.3c00689.
[35] A.Y. Lee, K. Yang, N.D. Anh, C. Park, S.M. Lee, T.G. Lee, M.S. Jeong, Raman study of D* band in graphene oxide and its correlation with reduction, Appl. Surf. Sci. 536 (2021) 147990, https://doi.org/10.1016/j.apsusc.2020.147990.
[36] J. Merida, M.T. Colomer, F. Rubio, M.A. Mazo, Highly porous carbon materials derived from silicon oxycarbides and effect of the pyrolysis temperature on their electrochemical response, Int. J. Mol. Sci. 24 (2023) 13868, https://doi.org/10.3390/ijms241813868.
[37] N. Talukder, Y. Wang, B.B. Nunna, E.S. Lee, Nitrogen-doped graphene nanomaterials for electrochemical catalysis/reactions: a review on chemical structures and stability, Carbon N. Y. 185 (2021) 198–214, https://doi.org/10.1016/j.carbon.2021.09.025.
[38] H. Gao, S. Wang, W.C. (Max) Cheong, K. Wang, H. Xu, A. Huang, J. Ma, J. Li, W.F. (Andy) Ip, K. San Hui, D.A. Dinh, X. Fan, F. Bin, F. Chen, K.N. Hui, Topological defect and sp3/sp2 carbon interface derived from ZIF-8 with linker vacancies for oxygen reduction reaction, Carbon N. Y. 203 (2023) 76–87, https://doi.org/10.1016/j.carbon.2022.10.030.
[39] S. Qu, Y. Yuan, X. Yang, H. Xu, A.K. Mohamed, J. Zhang, C. Zhao, L. Liu, B. Wang, X. Wang, J. Rinklebe, Y.C. Li, S. Wang, Carbon defects in biochar facilitated nitrogen doping: the significant role of pyridinic nitrogen in peroxymonosulfate activation and ciprofloxacin degradation, Chem. Eng. J. 441 (2022) 135864, https://doi.org/10.1016/j.cej.2022.135864.
[40] M. Smith, L. Scudiero, J. Espinal, J.S. McEwen, M. Garcia-Perez, Improving the deconvolution and interpretation of XPS spectra from chars by ab initio calculations, Carbon N. Y. 110 (2016) 155–171, https://doi.org/10.1016/j.carbon.2016.09.012.
[41] M. Ayiania, M. Smith, A.J.R. Hensley, L. Scudiero, J.S. McEwen, M. Garcia-Perez, Deconvoluting the XPS spectra for nitrogen-doped chars: an analysis from first principles, Carbon N. Y. 162 (2020) 528–544, https://doi.org/10.1016/j.carbon.2020.02.065.
[42] W. Yuan, G. Shi, Graphene-based gas sensors, J. Mater. Chem. A 1 (2013) 10078–10091, https://doi.org/10.1039/c3ta11774j.
[43] Y.S. Chang, F.K. Chen, D.C. Tsai, B.H. Kuo, F.S. Shieu, N-doped reduced graphene oxide for room-temperature NO gas sensors, Nature 11 (2021) 1–12, https://doi.org/10.1038/s41598-021-99883-9.
[44] G.V. Bianco, A. Sacchetti, M. Grande, A. D'Orazio, A. Milella, G. Bruno, Effective hole conductivity in nitrogen-doped CVD-graphene by singlet oxygen treatment under photoactivation conditions, Sci. Rep. 12 (2022) 1–11, https://doi.org/10.1038/s41598-022-12696-2.
[45] J. Hu, C. Yin, S. Xu, M. Cheng, T. Wei, Q. Liu, W. Li, Y. Ling, Y. Zhang, B. Liu, Enhanced room temperature NO2 sensing performance based on N-doped carbon nanosheets@ZnO nanoplates by morphology transition and white light illumination, Appl. Surf. Sci. 599 (2022) 153980, https://doi.org/10.1016/j.apsusc.2022.153980.
[46] J. López-Sánchez, Á. Peña, A. Serrano, A. Del Campo, Ó. Rodríguez De La Fuente, N. Carmona, D. Matatagui, M.D.C. Horrillo, J. Rubio-Zuazo, E. Navarro, P. Marín, Generation of defective few-layered graphene mesostructures by high-energy ball milling and their combination with FeSiCuNbB microwires for reinforcing microwave absorbing properties, ACS Appl. Mater. Interfaces 15 (2023) 3507–3521, https://doi.org/10.1021/acsami.2c19886.
[47] J.D. Aguilera, D. Arranz, A. Peña, P. Marín, M.C. Horrillo, P. de la Presa, D. Matatagui, Real-time monitoring of breath biomarkers using magnonic wireless sensor based on magnetic nanoparticles, Sens. Bio-Sens. Res. 43 (2024) 100629, https://doi.org/10.1016/j.sbsr.2024.100629.
[48] A. Peña, J.D. Aguilera, D. Matatagui, P. de la Presa, C. Horrillo, A. Hernando, P. Marín, Real-time monitoring of breath biomarkers with a magnetoelastic contactless gas sensor: a proof of concept, Biosensors 12 (2022) 1–17, https://doi.org/10.3390/bios12100871.
[49] P.M. Korusenko, V.V. Bolotov, S.N. Nesov, S.N. Povoroznyuk, I.P. Khailov, Changes of the electronic structure of the atoms of nitrogen in nitrogen-doped multiwalled carbon nanotubes under the influence of pulsed ion radiation, Nucl. Instrum. Methods Phys. Res. Sect. B Beam Interact. Mater. Atoms. 358 (2015) 131–135, https://doi.org/10.1016/j.nimb.2015.06.009.
[50] D. Haberer, A. Fedorov, V.K. Adamchuk, Nitrogen-doped graphene: efficient growth, structure, and electronic properties, Nano Lett. (2011) 5401–5407.
[51] S. van Dommele, A. Romero-Izquirdo, R. Brydson, K.P. de Jong, J.H. Bitter, Tuning nitrogen functionalities in catalytically grown nitrogen-containing carbon nanotubes, Carbon N. Y. 46 (2008) 138–148, https://doi.org/10.1016/j.carbon.2007.10.034.
[52] T. Thi Nguyet, L. Van Duy, N.C. Nam, D.Q. Dat, H. Nguyen, C.M. Hung, N. Van Duy, N.D. Hoa, Transition from p-type to n-type semiconductor in V_2O_5 nanowire-based gas sensors: synthesis and understanding of the sensing mechanism, Sensors Actuators B Chem. 424 (2025) 136841, https://doi.org/10.1016/j.snb.2024.136841.
[53] F.T. Johra, J.W. Lee, W.G. Jung, Facile and safe graphene preparation on solution based platform, J. Ind. Eng. Chem. 20 (2014) 2883–2887, https://doi.org/10.1016/j.jiec.2013.11.022.
[54] S. Uran, A. Alhani, C. Silva, Study of ultraviolet-visible light absorbance of exfoliated graphite forms, AIP Adv. 7 (2017) 035323, https://doi.org/10.1063/1.4979607.
[55] M.K. Rabchinskii, S.D. Saveliev, D.Y. Stolyarova, M. Brzhezinskaya, D.A. Kirilenko, M.V. Baidakova, S.A. Ryzhkov, V.V. Shnitov, V.V. Sysoev, P.N. Brunkov, Modulating nitrogen species via N-doping and post annealing of graphene derivatives: XPS and XAS examination, Carbon N. Y. 182 (2021) 593–604, https://doi.org/10.1016/j.carbon.2021.06.057.
[56] B. Ye, H. Tang, Q. Liu, W. Wang, L. Wang, J. Hu, Extended π-conjugated system in carbon nitride by incorporating pyridine rings and N vacancies for photocatalytic H2 evolution and H2O2 production, Carbon N. Y. 204 (2023) 465–474, https://doi.org/10.1016/j.carbon.2022.12.075.
[57] A. Govind, P. Bharathi, G. Mathankumar, M.K. Mohan, J. Archana, S. Harish, M. Navaneethan, Enhanced charge transfer in 2D carbon- rich g-C3N4 nanosheets for highly sensitive NO2 gas sensor applications, Diam. Relat. Mater. 128 (2022) 109205, https://doi.org/10.1016/j.diamond.2022.109205.
[58] B. Liu, X. Liu, Z. Yuan, Y. Jiang, Y. Su, J. Ma, H. Tai, A flexible NO2 gas sensor based on polypyrrole/nitrogen-doped multiwall carbon nanotube operating at room temperature, Sensors Actuators B Chem. 295 (2019) 86–92, https://doi.org/10.1016/j.snb.2019.05.065.
[59] X.H. Tian, T.Y. Zhou, Y. Meng, Y.M. Zhao, C. Shi, P.X. Hou, L.L. Zhang, C. Liu, H. M. Cheng, A flexible NO2 gas sensor based on single-wall carbon nanotube films doped with a high level of nitrogen, Molecules 27 (2022) 6523, https://doi.org/10.3390/molecules27196523.
[60] N.T. Hang, S. Zhang, W. Yang, Efficient exfoliation of g-C3N4 and NO2 sensing behavior of graphene/g-C3N4 nanocomposite, Sensors Actuators B Chem. 248 (2017) 940–948, https://doi.org/10.1016/j.snb.2017.01.199.

[61] S. Srivastava, P.K. Kashyap, V. Singh, T.D. Senguttuvan, B.K. Gupta, Nitrogen doped high quality CVD grown graphene as a fast responding NO2 gas sensor, New J. Chem. 42 (2018) 9550–9556, https://doi.org/10.1039/c8nj00885j.
[62] N. Hang, N.H. Hieu, L.T. Nhiem, Sensitive NO2 sensor based on silver nanowires-decorated monolayer graphene with assistance of UV illumination, J. Mater. Sci. Mater. Electron. 34 (2023) 1–11, https://doi.org/10.1007/s10854-022-09507-9.
[63] X. Yan, Y. Wu, R. Li, C. Shi, R. Moro, Y. Ma, L. Ma, High-performance UV-assisted NO2 sensor based on chemical vapor deposition graphene at room temperature, ACS Omega 4 (2019) 14179–14187, https://doi.org/10.1021/acsomega.9b00935.
[64] C.M. Yang, T.C. Chen, Y.C. Yang, M. Meyyappan, Annealing effect on UV-illuminated recovery in gas response of graphene-based NO2 sensors, RSC Adv. 9 (2019) 23343–23351, https://doi.org/10.1039/c9ra01295h.
[65] M. Zhou, W. Wang, J. Lu, Z. Ni, How defects influence the photoluminescence of TMDCs, Nano Res. 14 (2021) 29–39, https://doi.org/10.1007/s12274-020-3037-9.
[66] H. Ding, X.H. Li, X.B. Chen, J.S. Wei, X.B. Li, H.M. Xiong, Surface states of carbon dots and their influences on luminescence, J. Appl. Phys. 127 (2020) 231101, https://doi.org/10.1063/1.5143819.
[67] Y. Xu, M. Wu, Y. Liu, X.Z. Feng, X.B. Yin, X.W. He, Y.K. Zhang, Nitrogen-doped carbon dots: a facile and general preparation method, photoluminescence investigation, and imaging applications, Chem. - A Eur. J. 19 (2013) 2276–2283, https://doi.org/10.1002/chem.201203641.
[68] X. Niu, Y. Li, H. Shu, J. Wang, Revealing the underlying absorption and emission mechanism of nitrogen doped graphene quantum dots, Nanoscale 8 (2016) 19376–19382, https://doi.org/10.1039/c6nr06447g.
[69] O. Kozák, M. Sudolská, G. Pramanik, P. Cígler, M. Otyepka, R. Zbořil, Photoluminescent carbon nanostructures, Chem. Mater. 28 (2016) 4085–4128, https://doi.org/10.1021/acs.chemmater.6b01372.
[70] K.G. Nguyen, I.A. Baragau, R. Gromicova, A. Nicolaev, S.A.J. Thomson, A. Rennie, N.P. Power, M.T. Sajjad, S. Kellici, Investigating the effect of N-doping on carbon quantum dots structure, optical properties and metal ion screening, Sci. Rep. 12 (2022) 1–12, https://doi.org/10.1038/s41598-022-16893-x.
[71] K.G. Nguyen, M. Huš, I.A. Baragau, E. Puccinelli, J. Bowen, T. Heil, A. Nicolaev, D. Andrews, M.T. Sajjad, S. Dunn, S. Kellici, Controlling the optoelectronic properties of nitrogen-doped carbon quantum dots using biomass-derived precursors in a continuous flow system, Carbon N. Y. 230 (2024) 119623, https://doi.org/10.1016/j.carbon.2024.119623.
[72] J. Mooney, P. Kambhampati, Get the basics right: Jacobian conversion of wavelength and energy scales for quantitative analysis of emission spectra, J. Phys. Chem. Lett. 4 (2013) 3316–3318, https://doi.org/10.1021/jz401508t.
[73] C. de Passos, M.D. Merchán, M.M. Velázquez, Correlations between structure and photoluminescence properties in N-doped carbon nanoparticles, J. Sci. Adv. Mater. Devices 7 (2022) 100408, https://doi.org/10.1016/j.jsamd.2021.100408.
[74] H.J. Kleebe, Y.D. Blum, SiOC ceramic with high excess free carbon, J. Eur. Ceram. Soc. 28 (2008) 1037–1042, https://doi.org/10.1016/j.jeurceramsoc.2007.09.024.
[75] S. Brunauer, P.H. Emmett, E. Teller, Adsorption of gases in multimolecular layers, J. Am. Chem. Soc. 60 (1938) 309–319.
[76] B.E.P. Barrett, L.G. Joyner, P.P. Halenda, The determination of pore volume and area distributions in porous substances. I.Computations from nitrogen isotherms, J. Am. Chem. Soc. 73 (1951) 373–380.